Vision-Based Control and Stability Analysis of a Cable-Driven Parallel Robot

Zane Zake, François Chaumette, Nicolò Pedemonte, Stéphane Caro

Vision-Based Control and Stability Analysis of a Cable-Driven Parallel Robot

Zane Zake[1,2], François Chaumette[3], Nicolò Pedemonte[2], and Stéphane Caro[1,4]

***Abstract*— In Cable-Driven Parallel Robots (CDPRs) rigid links are substituted by flexible cables. This change in actuation allows for a large workspace with a high payload to weight ratio, among other appealing characteristics. However, the accuracy for such systems needs to be improved to truly outperform classical parallel robots. A possible and not yet well studied solution is the use of vision-based control for CDPRs. This paper deals with the stability analysis of such a control scheme with regard to uncertainties lying both in the analytical models and the experimental setup. Two CDPRs are analyzed as illustrative examples. The results obtained show the system's robustness with respect to uncertainties.**

I. INTRODUCTION

As the name suggests, a cable-driven parallel robot (CDPR) is a parallel robot that is actuated by flexible cables instead of rigid links. The main advantages of CDPRs are their large workspace (WS), low mass in motion, high velocity and acceleration capacity [1], and reconfigurability [2]. However, their accuracy should be substantially improved to meet a broader spectrum of industrial applications. In that sense, different approaches can be considered, such as the use of: (i) more precise, but more complex CDPR models [3]; (ii) force sensors to measure cable tensions [4]; (iii) angular position sensors to measure cable angle position [5]; and (iv) exteroceptive sensors, such as cameras, to measure where the robot is with respect to its environment [6] [7] [8].

Vision-based control is becoming more and more popular with the novel robot tasks, human-robot collaboration, and the need for robustness to different uncertainties. There are two main approaches of visual servoing: it can be either image-based or pose-based [9]. In the latter, using information from the image and some additional knowledge about the object (usually its model), the pose of the object with respect to (w.r.t.) the camera is retrieved. Then the control scheme is minimizing the difference between this acquired pose and the desired one. In image-based visual servoing, 2D image coordinates of the object or other image data are retrieved instead of a Cartesian pose. Here, the control algorithm is minimizing an error in the image space by comparing the desired and the current visual features.

It was found in [3] that even with a detailed CDPR model the experiments showed either a decrease or just a slight improvement in terms of accuracy. As a matter of fact, no matter the robot complexity, it is not possible to perfectly model the environment and predict the uncertainties. Hence, using visual data in the control loop is a good way to know precisely when the goal is reached, because it is directly perceived. This is attained by onlooking the robot with a camera fixed in the environment, which is the so called eye-to-hand configuration [6] [7]. Another option is to perceive the object of interest with a camera mounted on the moving platform (MP), namely eye-in-hand configuration [8]. The robot is actuated according to what is perceived in either of the configurations. Dallej *et al.* [6] proposed multiple control algorithms for large-scale CDPRs equipped with multiple fixed cameras. Chellal [7] used six infrared cameras to determine with high precision the position of the MP of a medium scale CDPR: INCA 6D. To the best of our knowledge, Remy *et al.* [8] have been the only ones using the eye-in-hand configuration and a single camera. A simplified 3-DOF CDPR generating translational motions only was used to successfully reach the vicinity of an object to be grasped. With the control strategy proposed in this paper, both the 3-DOF translational motions and 3-DOF rotational motions of the MP are handled, while using only one camera embedded in the MP.

The stability of CDPR usually deals with physical stability. For example, Carricato *et al.* investigated the stability of equilibrium for underconstrained CDPRs [10]. If one applies a force to the MP, the latter will easily move while keeping the cables taut and with the same lengths. While analyzing the stability of given CDPR the authors determined the final equilibrium pose, where the MP returns to once all perturbations are ceased. On the contrary, this paper focuses on stability analysis of CDPRs from a control viewpoint. Investigating the stability of a system is a way to analyze its sensitivity to different uncertainties, that is, to determine whether the system will converge accurately to its goal despite errors in its model [11]. Here, the largest ranges of perturbations for which the CDPR remains stable are assessed. Accordingly, this paper focuses on the stability analysis for a pose-based visual servoing control (PBVS) of a CDPR while determining its robustness to the various uncertainties involved in the system design. A planar CDPR and a spatial CDPR are considered as illustrative examples. Experimental results show the robustness of the system to

This work is supported by IRT Jules Verne (French Institute in Research and Technology in Advanced Manufacturing Technologies for Composite, Metallic and Hybrid Structures) in the framework of the PERFORM project.

[1]Laboratoire des Sciences du Numérique de Nantes, UMR CNRS 6004, 1, rue de la Noë, 44321 Nantes, France, Zane.Zake@ls2n.fr

[2]IRT Jules Verne, Chemin du Chaffault, 44340, Bouguenais, France, nicolo.pedemonte@irt-jules-verne.fr

[3]Inria, Univ Rennes, CNRS, IRISA, Rennes, France, Francois.Chaumette@inria.fr

[4]Centre National de la Recherche Scientifique (CNRS), 1, rue de la Noë, 44321 Nantes, France, stephane.caro@ls2n.fr

uncertainties and a better positioning accuracy w.r.t. classical model-based control.

This paper is organized as follows. Notations used throughout this paper are shown in Table I. Section II presents the vision-based control strategy for a CDPR, while focusing both on a planar and a spatial CDPR. Section III is dedicated to the stability analysis of both CDPRs. The experimental validation on a small-scale CDPR is shown in Section IV. Conclusions are drawn in Section V.

TABLE I

NOTATION USED THROUGHOUT THE PAPER

- $i = 1, \ldots, m$ denotes the cables, where m is the number of cables.
- Boldface lowercase characters denote vectors; boldface uppercase characters are matrices.
- $\mathcal{F}_b$, $\mathcal{F}_p$, $\mathcal{F}_c$, $\mathcal{F}_o$ denote the base, MP, camera and object frames respectively (resp.).
- ${}^i\boldsymbol{T}_j = \begin{bmatrix} {}^i\boldsymbol{R}_j & {}^i\boldsymbol{t}_j \\ \boldsymbol{0} & 1 \end{bmatrix}$ is the homogeneous transformation matrix from $\mathcal{F}_i$ to $\mathcal{F}_j$. It is either a (3×3)–matrix or a (4×4)–matrix in the planar and the spatial cases, resp.
- $\boldsymbol{A}^\dagger$ is the pseudo-inverse of $\boldsymbol{A}$.
- $\widehat{\boldsymbol{A}}$ and $\hat{\boldsymbol{e}}$ are the estimations of $\boldsymbol{A}$ and $\boldsymbol{e}$, resp.
- $[\boldsymbol{e}]_\times$ denotes the cross-product matrix of vector $\boldsymbol{e}$.
- $\mathrm{c}(\theta)$ and $\mathrm{s}(\theta)$ denotes the cosine and the sine of the angle θ.
- ${}^i\boldsymbol{a}$ is the vector $\boldsymbol{a}$ expressed in $\mathcal{F}_i$
- A_i and B_i are the exit and the anchor points of the ith cable, resp.
- ${}^b\boldsymbol{a}_i$ and ${}^p\boldsymbol{b}_i$ are the vectors pointing from origin of $\mathcal{F}_b$ and $\mathcal{F}_p$ and to A_i and B_i, resp.

II. VISION-BASED CONTROL OF A CDPR

In this work, a PBVS [9] is selected, with a camera mounted on the MP facing the object of interest. The following subsections detail the kinematics of CDPRs (II-A) and PBVS (II-B). First, the general equations are given and then, if distinction between the planar and the spatial cases is necessary, the details of the differences are also noted.

A. CDPR kinematics

Figures 1 and 2 show the schematics of a planar and a spatial CDPR, respectively.

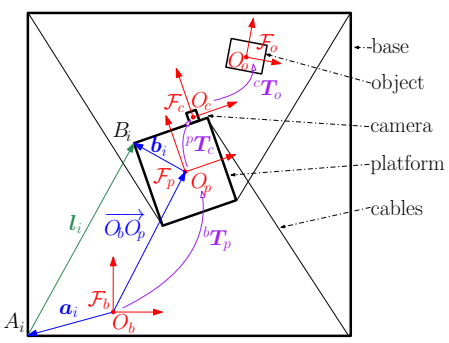

Fig. 1. Schematic of a planar CDPR with 4 cables, a camera mounted on its MP and an object in the WS

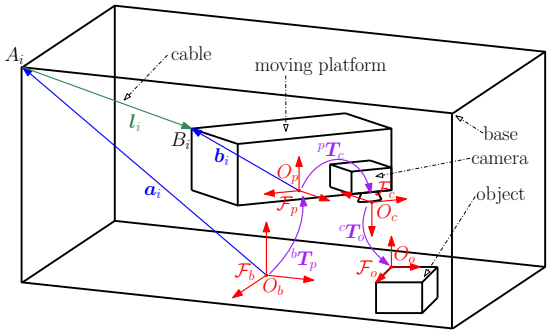

Fig. 2. Schematic of a spatial CDPR with eight cables, a camera mounted on its MP and an object in the WS

Since the camera is mounted on the MP, the transformation matrix between the respective frames ${}^p\boldsymbol{T}_c$ does not change with time, unlike the transformation matrix between the base and the platform frames ${}^b\boldsymbol{T}_p$, and the transformation matrix between the camera and the object frames ${}^c\boldsymbol{T}_o$.

The length l_i of the ith cable is the 2-norm of the vector $\overrightarrow{A_iB_i}$ pointing from A_i to B_i, namely,

$$l_i = \|\overrightarrow{A_iB_i}\|_2 \tag{1}$$

with

$$l_i\,{}^b\mathbf{u}_i = {}^b\overrightarrow{A_iB_i} = {}^b\boldsymbol{b}_i - {}^b\boldsymbol{a}_i = {}^b\boldsymbol{R}_p\,{}^p\boldsymbol{b}_i + {}^b\boldsymbol{t}_p - {}^b\boldsymbol{a}_i \tag{2}$$

where ${}^b\mathbf{u}_i$ is the unit vector of ${}^b\overrightarrow{A_iB_i}$ that is expressed as:

$${}^b\mathbf{u}_i = \frac{{}^b\overrightarrow{A_iB_i}}{\left\|{}^b\overrightarrow{A_iB_i}\right\|_2} = \frac{{}^b\boldsymbol{b}_i - {}^b\boldsymbol{a}_i}{\left\|{}^b\overrightarrow{A_iB_i}\right\|_2} = \frac{{}^b\boldsymbol{R}_p\,{}^p\boldsymbol{b}_i - {}^b\boldsymbol{a}_i + {}^b\boldsymbol{t}_p}{\left\|{}^b\overrightarrow{A_iB_i}\right\|_2} \tag{3}$$

and ${}^b\boldsymbol{R}_p$ and ${}^b\boldsymbol{t}_p$ are the rotation matrix and the translation vector from $\mathcal{F}_b$ to $\mathcal{F}_p$.

The cable velocities $\dot{l}_i$ are obtained upon differentiation of Eq. (2) w.r.t. time:

$$\dot{\boldsymbol{l}} = \boldsymbol{A}\,{}^b\mathbf{v}_p \tag{4}$$

where ${}^b\mathbf{v}_p$ is the Cartesian velocity of the MP expressed in $\mathcal{F}_b$, $\dot{\boldsymbol{l}}$ is the cable velocity vector, and $\boldsymbol{A}$ is the Forward Jacobian matrix of the CDPR, expressed as [13]:

$$\boldsymbol{A} = \begin{bmatrix} {}^b\mathbf{u}_1^T & ({}^b\boldsymbol{R}_p\,{}^p\boldsymbol{b}_1 \times {}^b\mathbf{u}_1)^T \\ \vdots & \vdots \\ {}^b\mathbf{u}_m^T & ({}^b\boldsymbol{R}_p\,{}^p\boldsymbol{b}_m \times {}^b\mathbf{u}_m)^T \end{bmatrix} \tag{5}$$

For a spatial CDPR with eight cables, the Jacobian $\boldsymbol{A}$ is a (8×6)–matrix. For a planar CDPR, $\boldsymbol{A}$ is a $(m\times3)$–matrix and takes the form:

$$\boldsymbol{A}_{pl} = \begin{bmatrix} {}^b\mathbf{u}_1^T & ({}^b\boldsymbol{R}_p\,{}^p\boldsymbol{b}_1)^T\boldsymbol{E}^T{}^b\mathbf{u}_1 \\ \vdots & \vdots \\ {}^b\mathbf{u}_m^T & ({}^b\boldsymbol{R}_p\,{}^p\boldsymbol{b}_m)^T\boldsymbol{E}^T{}^b\mathbf{u}_m \end{bmatrix} \tag{6}$$

with $\boldsymbol{E} = \begin{bmatrix} 0 & -1 \\ 1 & 0 \end{bmatrix}$.

B. Pose-based visual servoing

The control scheme considered in this paper is shown in Fig. 3. An image is acquired from the camera and fed to a computer vision algorithm, which in turn returns a 2D or 3D pose of the object ${}^{c}\boldsymbol{s}_o$ expressed in $\mathcal{F}_c$. It is compared to the desired pose ${}^{c^*}\boldsymbol{s}^*_o$, from which an error $\boldsymbol{e}$ is defined.

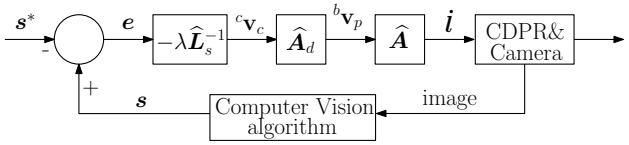

Fig. 3. Control scheme for pose-based visual servoing of a CDPR

For the spatial case $\boldsymbol{e} = [\boldsymbol{e}_t^T \ \boldsymbol{e}_\omega^T]^T$, where $\boldsymbol{e}_t = {}^{c}\boldsymbol{t}_o - {}^{c^*}\boldsymbol{t}_o = [e_x \ e_y \ e_z]^T$ and $\boldsymbol{e}_\omega = \mathbf{u}\theta$, $\mathbf{u}$ being the axis and θ the angle of the rotation matrix ${}^{c}\boldsymbol{R}_{c^*}$.

For the planar case $\boldsymbol{e}_{pl} = [\boldsymbol{e}_{t_{pl}}^T \ e_\theta]^T = [e_x \, e_y \, e_\theta]^T$.

To decrease the error $\boldsymbol{e}$, an exponential decoupled form is selected $\dot{\boldsymbol{e}} = -\lambda\boldsymbol{e}$ with a positive adaptive gain λ:

$$\lambda(x) = (\lambda_0 - \lambda_\infty)\mathrm{e}^{-(\dot{\lambda}_0/(\lambda_0-\lambda_\infty))x} + \lambda_\infty \tag{7}$$

where

- $x = ||\boldsymbol{e}||_2$ is the 2–norm of $\boldsymbol{e}$ at the current iteration
- $\lambda_0 = \lambda(0)$ is the gain for very small values of $||\boldsymbol{e}||_2$
- $\lambda_\infty = \lambda(\infty)$ is the gain for very high values of $||\boldsymbol{e}||_2$
- $\dot{\lambda}_0$ is the slope of λ at $||\boldsymbol{e}||_2 = 0$

The adaptive gain is computed at each iteration, depending on the current $||\boldsymbol{e}||_2$, in order to decrease the time-to-convergence [8].

Note that the error $\boldsymbol{e}$ tends towards zero when the actual object pose $\boldsymbol{s}$ converges to the desired object pose $\boldsymbol{s}^*$.

The relationship between $\dot{\boldsymbol{e}}$ and the Cartesian velocity of the camera ${}^{c}\mathbf{v}_c$, expressed in $\mathcal{F}_c$, is expressed as:

$$\dot{\boldsymbol{e}} = \boldsymbol{L}_{\boldsymbol{s}} \, {}^{c}\mathbf{v}_c \tag{8}$$

where $\boldsymbol{L}_{\boldsymbol{s}}$ is the interaction matrix and takes the following form for the spatial case [9]:

$$\boldsymbol{L}_{\boldsymbol{s}} = \begin{bmatrix} -\boldsymbol{I}_3 & [\boldsymbol{e}_t]_\times \\ \mathbf{0}_3 & -\boldsymbol{L}_\omega \end{bmatrix} \tag{9}$$

with:

$$\boldsymbol{L}_\omega(\mathbf{u},\theta) = \boldsymbol{I}_3 - \frac{\theta}{2}[\mathbf{u}]_\times + \Big(1 - \frac{\mathrm{sinc}(\theta)}{\mathrm{sinc}^2(\frac{\theta}{2})}\Big)[\mathbf{u}]_\times^2 \tag{10}$$

and $\mathrm{sinc}(\theta) = \sin(\theta)/\theta$

The determinant of matrix $\boldsymbol{L}_\omega(\mathbf{u},\theta)$ is

$$det(\boldsymbol{L}_\omega) = \frac{1}{\mathrm{sinc}^2(\theta/2)} \tag{11}$$

From Eq. (11), $\boldsymbol{L}_\omega$, and thus $\boldsymbol{L}_{\boldsymbol{s}}$, is singular if and only if (iff) $\theta = 2k\pi$ with $k \neq 0$. Note that the configurations leading to singular $\boldsymbol{L}_{\boldsymbol{s}}$ matrix are out of the manipulator WS.

For the planar case, (9) simplifies to:

$$\boldsymbol{L}_{\boldsymbol{s}_{pl}} = \begin{bmatrix} -1 & 0 & e_y \\ 0 & -1 & -e_x \\ 0 & 0 & -1 \end{bmatrix} \tag{12}$$

Finally, the instantaneous velocity of the camera in its own frame is expressed as a function of the pose error as follows:

$${}^{c}\mathbf{v}_c = -\lambda\widehat{\boldsymbol{L}}_{\boldsymbol{s}}^{-1}\boldsymbol{e} \tag{13}$$

where $\widehat{\boldsymbol{L}}_{\boldsymbol{s}}^{-1}$ is the inverse of an estimation of $\boldsymbol{L}_{\boldsymbol{s}}$. Note that we can directly use the inverse, because the interaction matrix is square and of full rank for PBVS [9].

C. Kinematics and vision

To combine the modeling shown in Sections II-A and II-B, the MP twist, expressed in $\mathcal{F}_b$, is defined as a function of the camera velocity, expressed in $\mathcal{F}_c$:

$${}^{b}\mathbf{v}_p = \boldsymbol{A}_d \, {}^{c}\mathbf{v}_c \tag{14}$$

where $\boldsymbol{A}_d$ is the adjoint matrix. Its expression differs from the spatial case to the planar case:

For the spatial case, the adjoint matrix takes the form [12]:

$$\boldsymbol{A}_d = \begin{bmatrix} {}^{b}\boldsymbol{R}_c & [{}^{b}\boldsymbol{t}_c]_\times \, {}^{b}\boldsymbol{R}_c \\ \mathbf{0}_3 & {}^{b}\boldsymbol{R}_c \end{bmatrix} \tag{15}$$

For the planar case, the adjoint matrix is expressed as [14]:

$$\boldsymbol{A}_{d_{pl}} = \begin{bmatrix} {}^{b}\boldsymbol{R}_c & \boldsymbol{E}^T \, {}^{b}\boldsymbol{t}_{pc} \\ 0 \quad 0 & 1 \end{bmatrix} = \begin{bmatrix} {}^{b}\boldsymbol{R}_p \, {}^{p}\boldsymbol{R}_c & \boldsymbol{E}^T \, {}^{b}\boldsymbol{R}_p \, {}^{p}\boldsymbol{t}_c \\ 0 \quad 0 & 1 \end{bmatrix} \tag{16}$$

where ${}^{b}\boldsymbol{t}_{pc} = {}^{b}\boldsymbol{R}_p \, {}^{p}\boldsymbol{t}_c$ and ${}^{p}\boldsymbol{t}_c$ is the vector from O_p to O_c.

III. Stability analysis

The stability analysis of a system aims to determine the level of uncertainties that is acceptable such that the corresponding system converges towards the goal state for sure. In this paper, Lyapunov analysis is used to assess the stability of the closed-loop visual servoing system [11].

From Eqs. (4), (8) and (14) the model is the following:

$$\dot{\boldsymbol{e}} = \boldsymbol{L}_{\boldsymbol{s}} \, \boldsymbol{A}_d^{-1} \boldsymbol{A}^\dagger \, \dot{\boldsymbol{l}} \tag{17}$$

Upon injecting (14) and (13) into (4), the output of the control scheme, that is, the cable velocity vector takes the form:

$$\dot{\boldsymbol{l}} = -\lambda \, \widehat{\boldsymbol{A}} \, \widehat{\boldsymbol{A}}_d \, \widehat{\boldsymbol{L}}_{\boldsymbol{s}}^{-1} \boldsymbol{e} \tag{18}$$

where $\widehat{\boldsymbol{A}}$ and $\widehat{\boldsymbol{A}}_d$ are the estimations of $\boldsymbol{A}$ and $\boldsymbol{A}_d$, resp. The following closed-loop equation is obtained from (17) and (18):

$$\dot{\boldsymbol{e}} = -\lambda \, \boldsymbol{L}_{\boldsymbol{s}} \, \boldsymbol{A}_d^{-1} \boldsymbol{A}^\dagger \widehat{\boldsymbol{A}} \, \widehat{\boldsymbol{A}}_d \, \widehat{\boldsymbol{L}}_{\boldsymbol{s}}^{-1} \boldsymbol{e} \tag{19}$$

From (19), the system stability criterion is defined as:

$$\boldsymbol{\Pi} = \boldsymbol{L}_{\boldsymbol{s}} \, \boldsymbol{A}_d^{-1} \boldsymbol{A}^\dagger \widehat{\boldsymbol{A}} \, \widehat{\boldsymbol{A}}_d \, \widehat{\boldsymbol{L}}_{\boldsymbol{s}}^{-1} > \mathbf{0}, \forall t \tag{20}$$

$\boldsymbol{\Pi} > \mathbf{0}$ is a sufficient condition to obtain global asymptotic stability (GAS). It can be seen from the closed-loop equation (19) that if $\boldsymbol{\Pi}$ is positive definite, then the control scheme will ensure an exponential convergence of the error $\boldsymbol{e}$ to $\mathbf{0}$. However, if it is negative then the error $\boldsymbol{e}$ will increase and the system may diverge from the goal.

This means that if the estimations of the Jacobian matrix $\widehat{\boldsymbol{A}}$, the adjoint matrix $\widehat{\boldsymbol{A}}_d$ and the interaction matrix $\widehat{\boldsymbol{L}}_{\boldsymbol{s}}^{-1}$ are not too coarse, $\boldsymbol{\Pi}$ will be near the identity matrix, and so positive definite, ensuring that the system is GAS.

Here, the stability analysis is performed separately for the planar and the spatial CDPRs. Section III-A deals with the stability analysis of the planar CDPR shown in Fig. 1. Section III-B is about the stability analysis of the spatial CDPR shown in Fig. 2, which turns out to be more complex.

First, only uncertainties in the vision system, i.e., uncertainties in object pose estimation, are taken into account (Stability Analysis I). Then, uncertainties in the pose of the camera w.r.t. $\mathcal{F}_p$ are considered (Stability Analysis II). Finally, the uncertainties in the MP pose w.r.t $\mathcal{F}_b$ and the errors in anchor points B_i are examined (Stability Analysis III).

A. Stability analysis of the planar CDPR

1) Stability Analysis I: While considering the errors in the vision system only, matrices $\widehat{\boldsymbol{A}}$ and $\widehat{\boldsymbol{A}}_d$ are assumed to be determined accurately. Thus, the stability criterion for the planar CDPR is simplified to:

$$\boldsymbol{\Pi}_{p1} = \boldsymbol{L}_{\boldsymbol{s}_{pl}} \widehat{\boldsymbol{L}}_{\boldsymbol{s}_{pl}}^{-1} = \begin{bmatrix} 1 & 0 & \hat{e}_y - e_y \\ 0 & 1 & e_x - \hat{e}_x \\ 0 & 0 & 1 \end{bmatrix} > 0 \tag{21}$$

The symmetric part of $\boldsymbol{\Pi}_{p1}$, named $\left(\boldsymbol{\Pi}_{p1}\right)_{Sym}$, is obtained as follows:

$$\left(\boldsymbol{\Pi}_{p1}\right)_{Sym} = \frac{1}{2}\left(\boldsymbol{L}_{\boldsymbol{s}_{pl}} \widehat{\boldsymbol{L}}_{\boldsymbol{s}_{pl}}^{-1} + \left(\boldsymbol{L}_{\boldsymbol{s}_{pl}} \widehat{\boldsymbol{L}}_{\boldsymbol{s}_{pl}}^{-1}\right)^T\right) =$$

$$= \begin{bmatrix} 1 & 0 & \frac{\hat{e}_y - e_y}{2} \\ 0 & 1 & \frac{e_x - \hat{e}_x}{2} \\ \frac{\hat{e}_y - e_y}{2} & \frac{e_x - \hat{e}_x}{2} & 1 \end{bmatrix} \tag{22}$$

Consequently, the eigenvalues of $\left(\boldsymbol{\Pi}_{p1}\right)_{Sym}$ are:

$$\begin{bmatrix} \lambda_1 \\ \lambda_2 \\ \lambda_3 \end{bmatrix} = \begin{bmatrix} \frac{\sqrt{(e_x - \hat{e}_x)^2 + (e_y - \hat{e}_y)^2}}{2} + 1 \\ -\frac{\sqrt{(e_x - \hat{e}_x)^2 + (e_y - \hat{e}_y)^2}}{2} + 1 \\ 1 \end{bmatrix} \tag{23}$$

For (21) to hold, the eigenvalues λ_1, λ_2, and λ_3 should all be positive [15]. Note that λ_1 is always positive, as the term under the square root is always positive. λ_2 will be positive iff the following condition holds true:

$$(e_x - \hat{e}_x)^2 + (e_y - \hat{e}_y)^2 < 4 \tag{24}$$

Since $\boldsymbol{e}_{pl} = \boldsymbol{s} - \boldsymbol{s}^*$ and $\hat{\boldsymbol{s}}^* = \boldsymbol{s}^*$, then (24) becomes:

$$(s_x - \hat{s}_x)^2 + (s_y - \hat{s}_y)^2 < 4 \tag{25}$$

Considering that the desired accuracy is centimetric (if not millimetric), then having a combined squared detection uncertainty lower that 4 m can be easily ensured in practice. Note that this is true for any CDPR because no uncertainty in the CDPR model parameters is considered here.

2) Stability Analysis II: Here, the uncertainties in the camera pose in $\mathcal{F}_p$ are considered along with the ones in the vision system. Accordingly, matrix $\boldsymbol{A}_{d_{pl}}$, expressed in (16), is considered in the stability criterion (20), which becomes:

$$\boldsymbol{\Pi}_{p2} = \boldsymbol{L}_{\boldsymbol{s}_{pl}} \boldsymbol{A}_{d_{pl}}^{-1} \widehat{\boldsymbol{A}}_{d_{pl}} \widehat{\boldsymbol{L}}_{\boldsymbol{s}_{pl}}^{-1} = \begin{bmatrix} \boldsymbol{R}_\psi & \begin{matrix} d_1 \\ d_2 \end{matrix} \\ \begin{matrix} 0 & 0 \end{matrix} & 1 \end{bmatrix} > 0 \tag{26}$$

where:

$$\boldsymbol{R}_\psi = {}^c\boldsymbol{R}_p \, {}^p\widehat{\boldsymbol{R}}_c = \begin{bmatrix} \mathrm{c}(\psi) & -\mathrm{s}(\psi) \\ \mathrm{s}(\psi) & \mathrm{c}(\psi) \end{bmatrix} \tag{27}$$

$$d_1 = \hat{e}_y \mathrm{c}(\psi) - e_y + \hat{e}_x \mathrm{s}(\psi) - \Delta t_y \mathrm{c}(\theta_{cp}) - \Delta t_x \mathrm{s}(\theta_{cp}) \tag{28}$$

$$d_2 = -\hat{e}_x \mathrm{c}(\psi) + e_x + \hat{e}_y \mathrm{s}(\psi) - \Delta t_y \mathrm{s}(\theta_{cp}) + \Delta t_x \mathrm{c}(\theta_{cp}) \tag{29}$$

with $\psi = \theta_{cp} - \hat{\theta}_{cp}$; $\Delta t_x = (t_x - \hat{t}_x)$ and $\Delta t_y = (t_y - \hat{t}_y)$

The eigenvalues of $\left(\boldsymbol{\Pi}_{p2}\right)_{Sym}$ are the following:

$$\begin{bmatrix} \lambda_1 \\ \lambda_2 \\ \lambda_3 \end{bmatrix} = \begin{bmatrix} \mathrm{c}(\psi) \\ \frac{\mathrm{c}(\psi) + 1 + \sqrt{(1 - \mathrm{c}(\psi))^2 + d_1^2 + d_2^2}}{2} \\ \frac{\mathrm{c}(\psi) + 1 - \sqrt{(1 - \mathrm{c}(\psi))^2 + d_1^2 + d_2^2}}{2} \end{bmatrix} \tag{30}$$

λ_1 is positive iff

$$|\psi| = |\theta_{cp} - \hat{\theta}_{cp}| < \pi/2 \tag{31}$$

λ_2 is always positive, because the term under the square root is always positive, given that (31) is held. Finally, due to the complexity of the expression, λ_3 is analyzed numerically.

In the numerical analysis it was found that a multitude of perturbation range combinations within system stability is possible. That is, there is not one single limit for each uncertainty, because the uncertainties do not affect the system independently. For this reason, it is possible to find different maximum values for the variables, depending on the other variable choices. Some examples are shown in Fig. 4, where each vertical line corresponds to one of the possible combinations. For instance, from Combination (Cb.) 2 the system will be stable if:

$$\begin{cases} |\boldsymbol{e}_{pl}| = \begin{cases} |e_x| = |s_x - s_x^*| \leqslant 5.0\,\mathrm{m} \\ |e_y| = |s_y - s_y^*| \leqslant 5.0\,\mathrm{m} \end{cases} \\ |\Delta \boldsymbol{e}_{pl}| = \begin{cases} |\Delta e_x| = |e_x - \hat{e}_x| \leqslant 0.5\,\mathrm{m} \\ |\Delta e_y| = |e_y - \hat{e}_y| \leqslant 0.5\,\mathrm{m} \end{cases} \\ |\Delta \boldsymbol{t}| = \begin{cases} |\Delta t_x| \leqslant 0.3\,\mathrm{m} \\ |\Delta t_y| \leqslant 0.3\,\mathrm{m} \end{cases} \\ |\Delta\theta| = |\psi| \leqslant 6^\circ \end{cases}$$

From Cb. 13, the system will be stable if:

$$\begin{cases} |\boldsymbol{e}_{pl}| = \begin{cases} |e_x| = |s_x - s_x^*| \leqslant 0.5\,\mathrm{m} \\ |e_y| = |s_y - s_y^*| \leqslant 0.5\,\mathrm{m} \end{cases} \\ |\Delta \boldsymbol{e}_{pl}| = \begin{cases} |\Delta e_x| = |e_x - \hat{e}_x| \leqslant 0.3\,\mathrm{m} \\ |\Delta e_y| = |e_y - \hat{e}_y| \leqslant 0.3\,\mathrm{m} \end{cases} \\ |\Delta \boldsymbol{t}| = \begin{cases} |\Delta t_x| \leqslant 0.2\,\mathrm{m} \\ |\Delta t_y| \leqslant 0.2\,\mathrm{m} \end{cases} \\ |\Delta\theta| = |\psi| \leqslant 61^\circ \end{cases}$$

It should be noted, that for any combination, each variable can take any value within the chosen limits. Therefore, it can be concluded that the system is exhibiting very strong robustness.

It should also be noted that at this level the stability analysis is still independent of the CDPR model. Although the estimation of camera pose in $\mathcal{F}_p$ is considered and ranges $\Delta \boldsymbol{t}$ and $\Delta\theta$ are found, they are not dependent on the actual ${}^p\boldsymbol{t}_c$ or θ. Therefore, the MP can take any size.

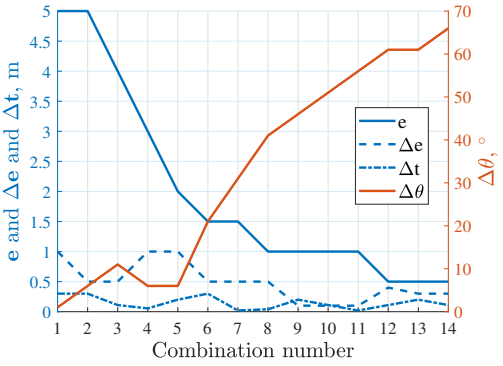

Fig. 4. Example of possible combinations of design variables ($\boldsymbol{e}$, $\Delta\boldsymbol{e}$, $\Delta\boldsymbol{t}$, $\Delta\theta$) for a stable system

3) Stability Analysis III: Finally, the uncertainties in the MP pose w.r.t. $\mathcal{F}_b$ and the errors in anchor points B_i are examined in addition to the previously mentioned ones. Here, the stability criterion (20) cannot be simplified. Due to its complexity, especially the pseudo-inverse of the Jacobian matrix $\boldsymbol{A}_{pl}^{\dagger}$, the stability analysis is performed numerically.

Some sets of variable ranges that ensure system stability are shown in Fig. 5. Considering the CDPR used for experimental validation of the spatial case, the WS size of the robot is supposed to be equal to 1 m ×1 m. The origin of $\mathcal{F}_b$ is located at the WS center. Similarly, due to the size of the existing MP, the maximum offset between the origins of $\mathcal{F}_p$ and $\mathcal{F}_c$ is equal to 0.055 m.

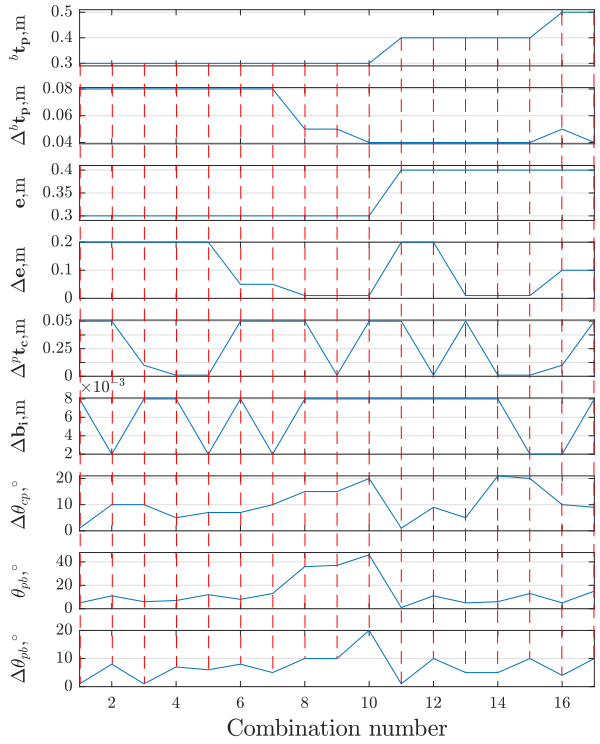

Fig. 5. Example of possible combinations of design variables (${}^b\boldsymbol{t}_p$, $\Delta{}^b\boldsymbol{t}_p$, $\boldsymbol{e}$, $\Delta\boldsymbol{e}$, $\Delta{}^p\boldsymbol{t}_c$, $\Delta{}^p\boldsymbol{b}_i$, $\Delta\theta_{cp}$, θ_{pb}, $\Delta\theta_{pb}$) for a stable system

Some other characteristics were also observed:

i) The smaller the actual working range ${}^b\boldsymbol{t}_p$ compared to WS, the larger the tolerated deviation $\Delta{}^b\boldsymbol{t}_p$.
ii) The difference between $\boldsymbol{e}$ and $\hat{\boldsymbol{e}}$ should always be smaller than $\boldsymbol{e}$ itself.
iii) ${}^p\boldsymbol{t}_c$ and θ_{cp} range do not have any effect on stability.
iv) Reducing $\Delta{}^p\boldsymbol{t}_c$ often leads to significant increase in the rotational range for θ_{pb}.
v) Similarly, reducing $\Delta\boldsymbol{b}_i$ allows having larger rotational errors.
vi) For $|{}^b\boldsymbol{t}_p| \leqslant 0.5$ m, the estimation of cable anchor points cannot be coarse.
vii) If $\Delta{}^b\boldsymbol{t}_p$ and $\Delta\boldsymbol{e}_{pl}$ are comparatively small, and the MP is not in the vicinity of the WS limits, platform could rotate up to 46°. The closer the MP to the center of the WS, the larger its range of rotation.

In conclusion, despite having so many input variables, the system is highly robust.

B. Stability analysis of the spatial CDPR

1) Stability Analysis I: Similarly as in Section III-A.1, when considering only the errors in the vision system, the stability criterion (20) simplifies to:

$$\boldsymbol{\Pi}_{s1} = \boldsymbol{L_s}\hat{\boldsymbol{L}}_{\boldsymbol{s}}^{-1} = \begin{bmatrix} \boldsymbol{I}_3 & -\Big([\boldsymbol{e}_t]_\times - [\hat{\boldsymbol{e}}_t]_\times\Big)\hat{\boldsymbol{L}}_\omega^{-1} \\ \boldsymbol{0}_3 & \boldsymbol{L}_\omega\hat{\boldsymbol{L}}_\omega^{-1} \end{bmatrix} > 0 \tag{32}$$

Since $\boldsymbol{\Pi}_{s1}$ is a (6×6)–matrix, the analytical stability analysis of spatial CDPRs turns out to be very complex. The numerical results are shown in Fig. 6.

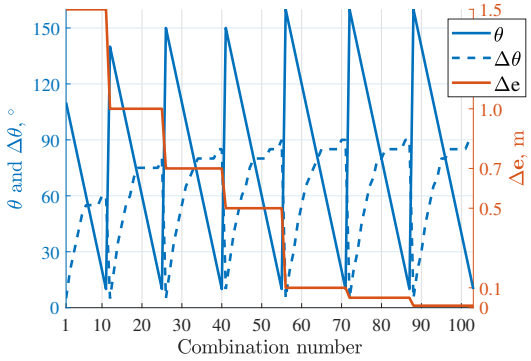

Fig. 6. Example of possible combinations of design variables ($\Delta\boldsymbol{e}$, θ, $\Delta\theta$)

Note that $\Delta\boldsymbol{e} = \boldsymbol{e} - \hat{\boldsymbol{e}} = \big(\boldsymbol{s} - \boldsymbol{s}^*\big) - \big(\hat{\boldsymbol{s}} + \boldsymbol{s}^*\big) = \boldsymbol{s} - \hat{\boldsymbol{s}}$.

Similarly to the stability analysis of the planar CDPR, the variable ranges are interdependent. It means that the lower $\Delta\boldsymbol{e}$, the higher the acceptable range for θ and/or $\Delta\theta$. The following maximum values were found: (i) $\Delta\boldsymbol{e}$ can be at most 1.5 m (Fig. 6 Cb.1 through 10); (ii) θ can be at most 160° (e.g. Cb. 56); (iii) $\Delta\theta$ can be at most 90° (e.g. Cb. 55).

2) Stability Analysis II: Here, as in Section III-A.2, only the Jacobian matrices disappear from the closed-loop equation (19); therefore, the stability criterion (20) becomes:

$$\boldsymbol{\Pi}_{s2} = \boldsymbol{L_s}\,\boldsymbol{A}_d^{-1}\,\hat{\boldsymbol{A}}_d\,\hat{\boldsymbol{L}}_{\boldsymbol{s}}^{-1} > 0 \tag{33}$$

with

$$\boldsymbol{\Pi}_{s2} = \begin{bmatrix} {}^c\boldsymbol{R}_p\,{}^p\hat{\boldsymbol{R}}_c & d_3 \\ \boldsymbol{0}_3 & \boldsymbol{L}_\omega\,{}^c\boldsymbol{R}_p\,{}^p\hat{\boldsymbol{R}}_c\hat{\boldsymbol{L}}_\omega^{-1} \end{bmatrix} \tag{34}$$

where $d_3 = \left({}^c\boldsymbol{R}_p\,{}^p\widehat{\boldsymbol{R}}_c[\hat{\boldsymbol{e}}_t]_\times - [\boldsymbol{e}_t]_\times\,{}^c\boldsymbol{R}_p\,{}^p\widehat{\boldsymbol{R}}_c + {}^c\boldsymbol{R}_p\,{}^p\boldsymbol{R}_b\left(\left[{}^b\boldsymbol{t}_c\right]_\times - \left[{}^b\hat{\boldsymbol{t}}_c\right]_\times\right){}^b\boldsymbol{R}_p\,{}^p\widehat{\boldsymbol{R}}_c\right)\widehat{\boldsymbol{L}}_\omega^{-1}$

Due to the high variability of the previous numerical analysis (Fig. 6), adding another two sets of spatial rotation makes such a graph useless. It means that there is an infinite number of possible combinations of axis-angle $\boldsymbol{u}\theta$ with rotation matrices ${}^b\boldsymbol{R}_p$, ${}^p\boldsymbol{R}_c$, and ${}^p\widehat{\boldsymbol{R}}_c$. Looking at (34), it is clear that the rotations are not acting independently. Conversely, their interaction affects the stability of the system.

However it is possible to make some conclusions for the other variables.

i) The system will be stable if $\Delta\boldsymbol{e} \leqslant \boldsymbol{e}$.
ii) The lower $\Delta\boldsymbol{e}$, the larger the available rotational range.
iii) Finally, $\Delta^p\boldsymbol{t}_c$ does not affect system stability, as long as it is reasonably small (tested range was up to 0.2 m).

Note that the Jacobian matrix has not been considered as it is assumed to be precisely estimated. Accordingly, the stability criterion is affected only by the uncertainties in the transformation matrix ${}^p\boldsymbol{T}_c$ and by the vision algorithm. It appears that the system stability is little sensitive to uncertainties in ${}^p\boldsymbol{T}_c$. Therefore, the object pose estimation should be the primary focus for reducing perturbations.

3) Stability Analysis III: Finally, the uncertainties in all the matrices $\boldsymbol{L_s}$, $\boldsymbol{A}$, and $\boldsymbol{A}_d$ are taken into account. The stability criterion is kept in its full unsimplified form (20).

Some variable range examples to ensure system stability are shown in Fig. 7. For readability, rotation matrix ${}^b\boldsymbol{R}_p$ has been transformed to Euler angles and is noted as RPY.

Similarly to Section III-A.3, the effect of uncertainties in the CDPR model on the stability of the system is investigated. The model of ACROBOT, the CDPR prototype shown in Fig. 8 is used. This model considers the Cartesian coordinates of exit points A_i and connection points B_i. The WS size is $1 \times 1 \times 1$ m. It is assumed that $\Delta b_{x,i} = \Delta b_{y,i} = \Delta b_{z,i} = 0.008$ m.

Some noteworthy characteristics were observed in addition to (i)-(ii) of Section III-A.3 :

i) The smaller $\Delta^b\boldsymbol{t}_p$ or $\Delta^p\boldsymbol{t}_c$, the higher the range of rotation of the MP, especially about Z axis.
ii) The lower the rotation of the MP about Z axis, the higher its rotation about X and Y axis.
iii) System stability is heavily dependent on MP position in the base frame $\mathcal{F}_b$. The closer the MP to the origin of $\mathcal{F}_b$, the larger $\Delta^b\boldsymbol{t}_p$ while keeping the CDPR stable.
iv) Similarly, the closer the MP to the origin of $\mathcal{F}_b$, the larger the range of rotation.

Therefore, the presented system is robust to large uncertainties, including those in the robot model. As a conclusion, if the robot model is not defined accurately, then using vision-based control will give lead to better robot accuracy than using model-based control of CDPRs.

IV. Experimental Validation

A. Experimental Setup

To validate the stability analysis presented above, a small spatial CDPR, named ACROBOT and shown in Fig. 8, is used. It is assembled in a suspended configuration.

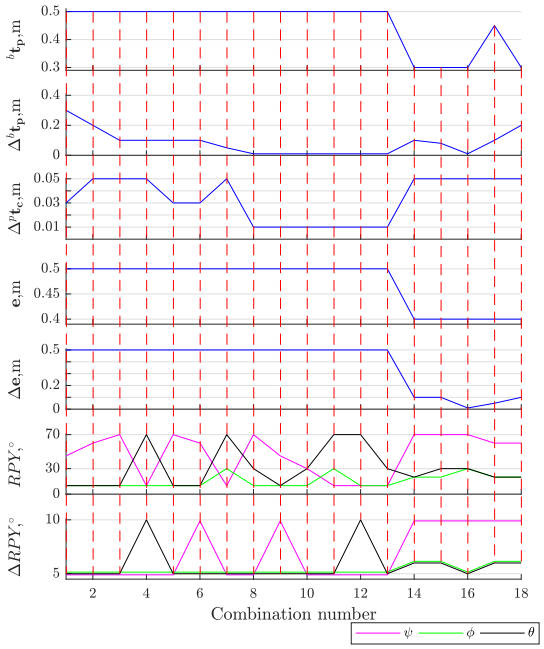

Fig. 7. Example of possible combinations of design variables (${}^b\boldsymbol{t}_p$, $\Delta^b\boldsymbol{t}_p$, $\Delta^p\boldsymbol{t}_c$, $\boldsymbol{e}$, $\Delta\boldsymbol{e}$, ϕ, θ, ψ, $\Delta\phi$, $\Delta\theta$, $\Delta\psi$)

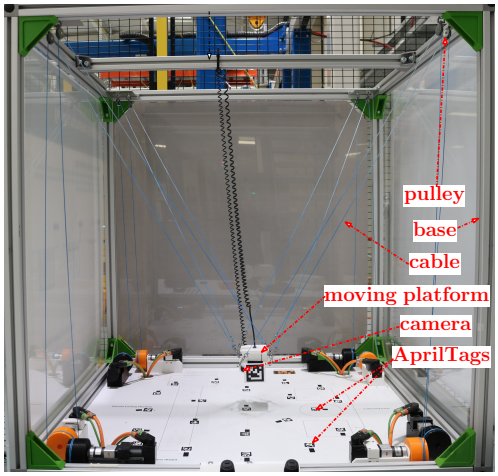

Fig. 8. ACROBOT: a CDPR prototype located at IRT Jules Verne, Nantes

For the visual servoing, a simple webcam Media-tech AUTOPIX MT4018 is used. It is mounted on the MP of the ACROBOT (eye-in-hand configuration) facing the ground.

To simplify the computer vision part, AprilTags [16] are used as objects. They are recognized and localized with algorithms available in ViSP library [17]. These tags are put in various places on the ground as shown in Fig. 8. The robot can then be controlled to reach any one of these tags as long as it is in the field of view.

B. Experimental Results

The sources of known "base" uncertainties are:

i) Cable anchor points B_i cannot be precisely measured due to the mechanical connections between the cables and MP. In the model B_i is considered as a point,

while in experiments it is actually a point located on a $\varnothing 0.016$ m sphere around its nominal location;

ii) To be able to compute the Forward Jacobian as in (5), we need to know ${}^b\boldsymbol{R}_p$ and cable unit vectors ${}^b\mathbf{u}_i$ from (3), which depend on actual pose of the MP in the base frame expressed by the transformation matrix ${}^b\boldsymbol{T}_p$. It is complex to determine ${}^b\boldsymbol{T}_p$, therefore an estimation is made based on the camera velocity ${}^c\mathbf{v}_c$ using the exponential map [14]:

$$({}^b\boldsymbol{T}_p)_{t+\Delta t} = ({}^b\boldsymbol{T}_c)_{t+\Delta t}\,{}^c\boldsymbol{T}_p = ({}^b\boldsymbol{T}_c)_t \exp^{({}^c\mathbf{v}_c,\Delta t)}\,{}^c\boldsymbol{T}_p \tag{35}$$

Note that ${}^c\mathbf{v}_c$ is the output of the control scheme, and that $({}^b\boldsymbol{T}_p)_{t=0}$ is an estimation itself[1], because the initial MP pose is not precisely known. Therefore, $({}^b\boldsymbol{T}_p)_{t+\Delta t}$ is a coarse approximation.

iii) The auto-focus option of the chosen camera leads to the image being zoomed in and out. This is not taken into account, when the AprilTag is being detected, leading to an imprecise computed object pose $\boldsymbol{s}$.

Despite these uncertainties, the experiments show that they do not destabilize the system.

Three types of experiments were made. First, with the aforementioned "base" uncertainties. Second, adding voluntary perturbations within the stability bounds exhibited in the previous section. And third, adding perturbations that do not respect these bounds. The perturbation input values were taken from Combination 18 in Fig. 7.

The experiments were defined as follows: initial MP pose is $\mathbf{p}_s = \begin{bmatrix}0.097 & -0.026 & 0.323 & 20^\circ & -20^\circ & 45^\circ\end{bmatrix}$. The final MP pose is $\mathbf{p}_f = \begin{bmatrix}0.35 & 0.28 & 0.06 & 0^\circ & 0^\circ & 0^\circ\end{bmatrix}$. Additional tolerable perturbations: 0.1 m for each component of $\Delta{}^b\boldsymbol{t}_p$; 5° about each axis. Additional perturbations out of bounds of stability: 0.2 m for each component of $\Delta{}^b\boldsymbol{t}_p$; 10° about each axis.

The experimental results are shown in Fig. 9 (see also the accompanying video). The AprilTag trajectories are shown in the first column. The error $\boldsymbol{e}$ over time is given in the second column. The main conclusions are:

i) Despite the noise in the "base" case, a good decoupled exponential decrease of $\boldsymbol{e}$ can be observed in Fig. 9(b).

ii) The trajectory of the center of the target is not a straight line due to "base" perturbations (Fig. 9(a)).

iii) Once tolerable perturbations are added, the trajectory becomes disrupted (see Fig. 9(c)) and the convergence time increases (see Fig. 9(d)), but the system still converges to its goal.

iv) Perturbations in the last case are out of the stability bounds. Hence, the AprilTag leaves the image instead of converging to its center as shown in Fig. 9(e).

To compare the vision-based control method of CDPRs to other existing methods, it was chosen to implement a simple model-based control. Given the previously mentioned initial

[1]For this CDPR, the initial pose was defined at the center of the WS, which itself was measured by hand with a measurement error of ± 2 cm along X and Y axes, resp. This allows to avoid the computation of forward kinematics, which is a difficult task, since it requires a good knowledge of cable lengths and tensions.

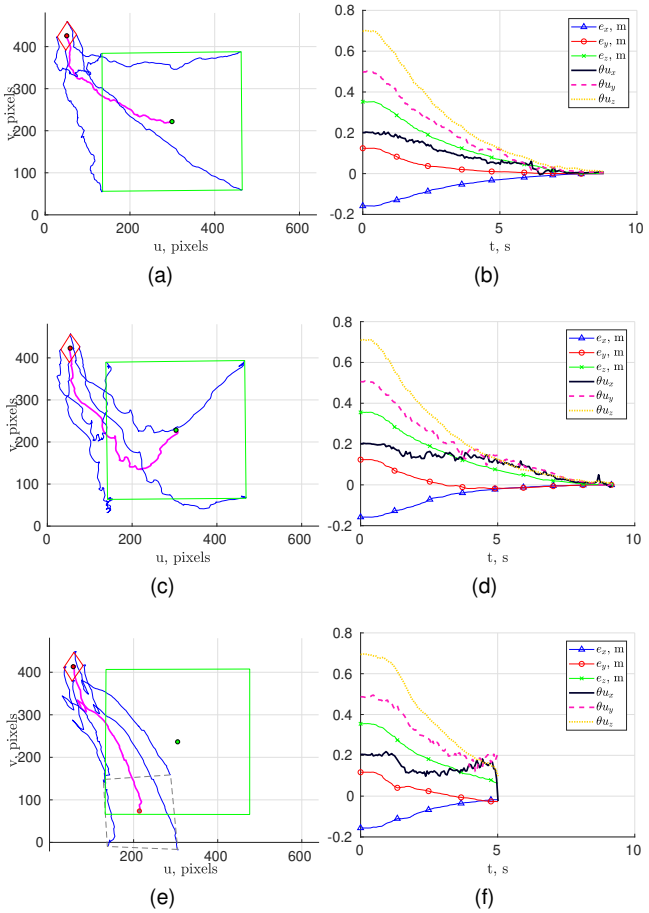

Fig. 9. CDPR behavior depending on added perturbations. (a) and (b): the AprilTag trajectory and error $\boldsymbol{e}$ over time for the "base" case; system is stable. (c) and (d): the AprilTag trajectory and error $\boldsymbol{e}$ over time when tolerable perturbations are added; system is stable. (e) and (f): the AprilTag trajectory and error $\boldsymbol{e}$ over time when significant perturbations out of bounds of stability are added; system is not stable.

and final MP poses, $\mathbf{p}_s$ and $\mathbf{p}_f$ resp., a trajectory is generated using a fifth-order polynomial [18]:

$$s = bt^5 + ct^4 + dt^3 + et^2 + ft + g \tag{36}$$

while considering the following conditions at the start and at the end of the trajectory: $s(t_s) = \dot{s}(t_s) = \ddot{s}(t_s) = 0$, $s(t_f) = 1$, and $\dot{s}(t_f) = \ddot{s}(t_f) = 0$.

The MP position ${}^b\boldsymbol{t}_p$ and translational velocity ${}^b\boldsymbol{v}_p$ as a function of time are expressed as:

$$\begin{cases} {}^b\boldsymbol{t}_p(t) = \boldsymbol{t}_s + (\boldsymbol{t}_f - \boldsymbol{t}_s)\, s(t) \\ {}^b\boldsymbol{v}_p(t) = (\boldsymbol{t}_f - \boldsymbol{t}_s)\, \dot{s}(t) \end{cases} \tag{37}$$

where $\boldsymbol{t}_s$ and $\boldsymbol{t}_f$ are the translational parts of $\mathbf{p}_s$ and $\mathbf{p}_f$, resp.

As for the rotation, we start from ${}^{p_s}\boldsymbol{R}_{p_f} = {}^b\boldsymbol{R}_{p_s}^T\,{}^b\boldsymbol{R}_{p_f}$, where ${}^b\boldsymbol{R}_{p_s}$ and ${}^b\boldsymbol{R}_{p_f}$ are the rotation matrices for poses $\mathbf{p}_s$ and $\mathbf{p}_f$, resp. When changed to axis-angle representation, ${}^{p_s}\boldsymbol{R}_{p_f}$ is noted as $\theta_p\mathbf{u}_p$. Here, the unit vector $\mathbf{u}$ is constant and the angle θ_p is a function of time $\theta_p(t) = \theta_p s(t)$, which corresponds to a rotation matrix ${}^{p_s}\boldsymbol{R}_{p_{curr}}$ and allows us to compute the current rotation matrix of the MP:

$${}^b\boldsymbol{R}_{p_{curr}} = {}^b\boldsymbol{R}_{p_s}\,{}^{p_s}\boldsymbol{R}_{p_{curr}} \tag{38}$$

Finally, the angular velocity ${}^b\boldsymbol{\omega}_p$ is computed as:

$$ {}^b\boldsymbol{\omega}_p(t) = \theta_p \mathbf{u}_p \dot{s}(t) \tag{39} $$

From the estimation of the MP pose through (37) and (38), it is possible to update the estimated Jacobian matrix $\widehat{\boldsymbol{A}}$. Then the cable velocities are computed as:

$$ \dot{\boldsymbol{l}} = \widehat{\boldsymbol{A}}\, {}^b\mathbf{v}_p(t) \tag{40} $$

where ${}^b\mathbf{v}_p(t) = \begin{bmatrix} {}^b\boldsymbol{v}_p^T(t) & {}^b\boldsymbol{\omega}_p^T(t) \end{bmatrix}^T$

Figure 10 shows the final pose of the MP. It appears that no matter the additional perturbations, the MP reaches the same pose with PBVS control as seen in Figs. 10(a) and 10(c). On the contrary, using model-based control the final MP pose is far from the targeted one for both the "base" case (see Fig. 10(b)) and the "perturbed" one (see Fig. 10(d)). Thus, CDPR model-based control is highly sensitive to uncertainties in the robot model. On the contrary, PBVS control turns out to be much more robust to perturbations. Indeed, as long as the system is stable, any uncertainty in the model has an effect on the transient phase, namely, the trajectory performed to reach the goal, but not on the final reached pose, which makes a clear difference in terms of accuracy between vision-based control and pure model-based control.

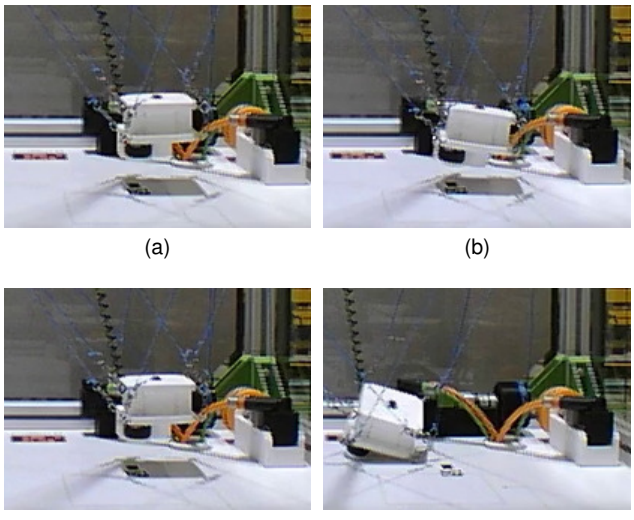

Fig. 10. MP pose at the end of a prescribed trajectory: the "base case" with (a) PBVS control and (b) Model-based control; the "perturbed" case with (c) PBVS control and (d) Model-based control

V. Conclusions

This paper proposed a method to analyze the stability of Cable-Driven Parallel Robots (CDPRs) under vision-based control. First, the stability of a planar CDPR was evaluated analytically when possible, numerically otherwise. Then, the stability of a spatial CDPR was assessed and experimentally tested. Here, the stability is a function of the uncertainties in the system. Different combinations of uncertainty ranges that guarantee the CDPR stability were determined.

From the analysis carried out in this paper, it turns out that a CDPR with a Pose-Based Visual Servoing (PBVS) control is little sensitive to uncertainties in the robot model. Since the object of interest is observed with a PBVS control, it is possible to know whether the desired pose has been reached or not. It means that no matter the amount of perturbations in the system, the moving-platform (MP) will always reach its targeted pose as long as the system is stable.

As a consequence, with a PBVS control the CDPR accuracy only depends on camera quality and the goal thresholding algorithm. Therefore, vision-based control is a good alternative to model-based control to improve the accuracy of CDPRs.

Later on, a PBVS control will be implemented on a large semi-industrial CDPR located at IRT Jules Verne and its stability will be studied. Image-Based Visual Servoing (IBVS) will be considered instead of PBVS, and their robustness will be compared. Finally, real objects will be used instead of AprilTags to increase the uncertainties in the vision system.

References

[1] S. Kawamura, W. Choe, S. Tanaka, and S. R. Pandian, "Development of an Ultrahigh Speed Robot Falcon Using Wire Driven System", in *ICRA*, pp. 215–220, IEEE, 1995.

[2] L. Gagliardini, S. Caro, M. Gouttefarde, and A. Girin, "Discrete Reconfiguration Planning for Cable-Driven Parallel Robots", in *Mechanism and Machine Theory*, vol. 100, pp. 313–337, 2016.

[3] V. L. Schmidt, "Modeling Techniques and Reliable Real-Time Implementation of Kinematics for Cable-Driven Parallel Robots using Polymer Fiber Cables", Ph.D. dissertation, Fraunhofer Verlag, Stuttgart, Germany, 2017.

[4] E. Picard, S. Caro, F. Claveau, and F. Plestan, "Pulleys and Force Sensors Influence on Payload Estimation of Cable-Driven Parallel Robots", in *Proceedings - IEEE/RSJ Int. Conf. on Intelligent Robots and Systems (IROS)*, Madrid, Spain, October, 1–5 2018.

[5] A. Fortin-Côté, P. Cardou, A. Campeau-Lecours, "Improving Cable-Driven Parallel Robot Accuracy Through Angular Position Sensors", in *IEEE/RSJ Int. Conf on Intelligent Robots and Systems (IROS)*, pp. 4350–4355, 2016.

[6] T. Dallej, M. Gouttefarde, N. Andreff, R.Dahmouche, and P. Martinet, "Vision-Based Modeling and Control of Large-Dimension Cable-Driven Parallel Robots", in *IEEE/RSJ Int. Conf. on Intelligent Robots and Systems (IROS)*, pp. 1581–1586, 2012.

[7] R. Chellal, L. Cuvillon, and E. Laroche, "A Kinematic Vision-Based Position Control of a 6-DoF Cable-Driven Parallel Robot", in *Cable-Driven Parallel Robots*, pp. 213–225, Springer, Cham, 2015.

[8] R. Ramadour, F. Chaumette, and J.-P. Merlet, "Grasping Objects With a Cable-Driven Parallel Robot Designed for Transfer Operation by Visual Servoing", in *ICRA*, pp. 4463–4468, IEEE, 2014.

[9] F. Chaumette, S. Hutchinson, "Visual servo Control I. Basic Approaches", in *IEEE Robotcs & Automation Magazine*, vol. 13, no. 4, pp. 82–90, 2006.

[10] M. Carricato, J.-P. Merlet, "Stability analysis of underconstrained cable-driven parallel robots", in *IEEE Transactions on Robotics*, vol. 29, no. 1, pp. 288–296, 2013.

[11] H. K. Khalil, Nonlinear systems, Macmillan publishing Co., 2nd ed., New York 1996.

[12] W. Khalil, E. Dombre, "Modeling, Identification and Control of Robots", Butterworth-Heinemann, 2004, pp. 13–29.

[13] A. Pott, "Cable-Driven Parallel Robots: Theory and Application", vol. 120., Springer, 2018, pp. 52–56.

[14] E. Eade, "Lie groups for computer vision", 2014.

[15] C.R. Johnson, "Positive definite matrices", in *The American Mathematical Monthly*, vol. 77, no. 3, pp. 259–264, 1970.

[16] E. Olson, "AprilTag: A robust and flexible visual fiducial system", in *ICRA*, pp. 3400–3407, IEEE, 2011.

[17] É. Marchand, F. Spindler, F. Chaumette, "ViSP for visual servoing: a generic software platform with a wide class of robot control skills", in *IEEE Robotics & Automation Magazine*, vol. 12, no. 4, pp. 40–52, 2005.

[18] S. Briot, S. Caro, and C. Germain, "Design Procedure for a Fast and Accurate Parallel Manipulator, in*ASME Journal of Mechanisms and Robotics*, vol. 9, no. 6, 061012, 2017.